Electrodeposition of an iron thin film with compact and smooth morphology using an ethereal electrolyte

AUTHOR(S):

Zhang, Zelei; Kitada, Atsushi; Fukami, Kazuhiro; Yao, Zhengjun; Murase, Kuniaki

CITATION:

Zhang, Zelei ...[et al]. Electrodeposition of an iron thin film with compact and smooth morphology using an ethereal electrolyte. Electrochimica Acta 2020, 348: 136289.

ISSUE DATE:

2020-07-10

URL:

http://hdl.handle.net/2433/255858

Electrochimica Acta 348 (2020) 136289

Contents lists available at ScienceDirect

Electrochimica Acta

journal homepage: www.elsevier.com/locate/electacta

Electrodeposition of an iron thin film with compact and smooth morphology using an ethereal electrolyte

Zelei Zhang [a, b], Atsushi Kitada [b, *], Kazuhiro Fukami [b], Zhengjun Yao [a], Kuniaki Murase [b]

[a] College of Material Science and Technology, Nanjing University of Aeronautics and Astronautics, Nanjing, 210016, China
[b] Department of Materials Science and Engineering, Kyoto University, Kyoto, 606-8501, Japan

ARTICLE INFO

Article history:
Received 17 February 2020
Received in revised form
17 April 2020
Accepted 21 April 2020
Available online 25 April 2020

Keywords:
Iron electrodeposition
Surface morphology
Thin film
Nucleation mechanism
Ethereal electrolyte

ABSTRACT

Electrodeposition of iron (Fe) from an ethereal solution was investigated. The bath consisted of ferrous chloride ($FeCl_2$), diglyme (G2), and aluminum chloride ($AlCl_3$), in which iron species were estimated to be $[Fe(G2)_2]^{2+}$ complex cations. The effect of hydrogen gas evolution on the morphology of iron deposits was determined by comparing common aqueous electrolytes. An Fe thin film was fabricated using the $FeCl_2$–G2–$AlCl_3$ bath without the influence of hydrogen gas evolution, and the nucleation of Fe was explained by an instantaneous nucleation mechanism. As a result, the surface morphology of the Fe thin film was compact and smooth compared with the cases of aqueous and other nonaqueous electrolytes.

1. Introduction

Iron (Fe) is one of the least expensive and most abundant elements. Metallic Fe shows ferromagnetism, high electrical conductivity, and other advantageous mechanical properties. Therefore, Fe thin film has been well-studied and has many proposed applications in electronics and spintronics, such as magnetic memory and electromagnetic shielding [1–3]. The giant magnetoresistance effect was discovered originally in Fe/Cr multilayers [4]. Ultrahigh-vacuum techniques are usually used to fabricate Fe thin films [5,6]. An electrodeposition method for thin films can be an alternative to ultrahigh-vacuum techniques, because the costs involved are relatively low.

The electrodeposition of an Fe thin film from aqueous solutions has been studied extensively [7–14]. Because the standard potential of the Fe^{2+}/Fe^0 deposition isotherm is more negative than that of the hydrogen evolution reaction — −0.44 V vs. a standard hydrogen electrode (SHE) — the electrodeposition of Fe is inevitably accompanied by side reactions [10]. The H_2 evolution results in a local pH increase near the cathode, forming iron hydroxide or iron hydroxy-chloride, and thereby the deposits are contaminated [11]. In addition, the hydrogen bubbles attached to the deposits inhibit the nucleation and growth of Fe deposits, resulting in a noncompact and rough surface morphology [11–13]. To prevent the formation of iron hydroxide, the pH of Fe electroplating baths should be lower than 3.5 [14]. Meanwhile, a pH buffer is necessary to stabilize the pH values during electrodeposition [15,16].

Nonaqueous baths without active protons are advantageous over conventional aqueous baths, in that H_2 gas evolution can be prevented. There are several studies on Fe electrodeposition from nonaqueous baths, including deep eutectic solvents and ionic liquids [17–21]. The Fe nanoparticles have been obtained from choline chloride (ChCl)–urea with $FeCl_3$ [17] and an ionic liquid $AlCl_3$–1-methyl-3-butylimidazolium chloride with electrochemically-dissolved Fe^{2+} [18], respectively. In ChCl–urea–$FeCl_2$ [19] and ChCl–ethylene glycol–$FeCl_2$ [20] baths, coarse Fe deposits grew on glassy carbon electrode through a progressive nucleation mechanism. Air- and water-stable ionic liquids composed of *N*-butyl-*N*-methylpyrrolidinium (BMP) cation and amide anions with $FeCl_2$ have also been used to electrodeposit Fe [21].

However, a compact Fe thin film with a smooth surface deposited from nonaqueous electrolytes has not been established. Fe thin films that are not compact are not suitable for many applications. In this work, a nonaqueous electrolyte for fabricating a compact and smooth Fe thin film is investigated. A relatively safe and cost-effective organic solvent, i.e., a high-boiling-point ether, diglyme

* Corresponding author.
E-mail address: kitada.atsushi.3r@kyoto-u.ac.jp (A. Kitada).

https://doi.org/10.1016/j.electacta.2020.136289

(G2), is used [22]. The dissolved chemical species and the electrodeposition mechanism are discussed.

2. Experimental

2.1. Reagents and bath preparation

G2 and ferrous chloride ($FeCl_2$) were purchased from Kanto Chemical Co. and FUJIFILM Wako Pure Chemical Co., respectively. High-purity aluminum chloride ($AlCl_3$) was supplied by Nippon Light Metal Co. The water content in the G2 solvent was less than 25 ppm after drying using molecular sieves. All baths were prepared in an Ar-filled glovebox with H_2O and O_2 contents of less than 5 ppm. The mixing ratio of $AlCl_3$–G2 solution was 1:5 by mole. Different concentrations for $FeCl_2$ in $AlCl_3$–G2 solution were prepared.

For the aqueous electrolytes, the $FeCl_2$ concentration varied from 0.025 mol dm^{-3} to 0.5 mol dm^{-3}. Based on previous research [13], some additives, including sodium chloride (NaCl, 0.7 mol dm^{-3}), boric acid (H_3BO_3, 0.4 mol dm^{-3}), saccharin (0.0075 mol dm^{-3}), and L-ascorbic acid (0.05 mol dm^{-3}), were added into 0.2 mol dm^{-3} $FeCl_2$ aqueous solution. Prior to the experiments, the aqueous electrolytes were purged with N_2 for 2 h to decrease the O_2 content. The pH of the electrolytes was adjusted to 3.0 using HCl or NaOH solutions.

2.2. Bath characterization

The electrolyte was sealed with a septum in the glovebox, which made it possible to perform viscosity measurements in an Ar atmosphere. The viscosity of the electrolytes was determined using an EMS Viscometer (EMS-1000, Kyoto Electronics Manufacturing

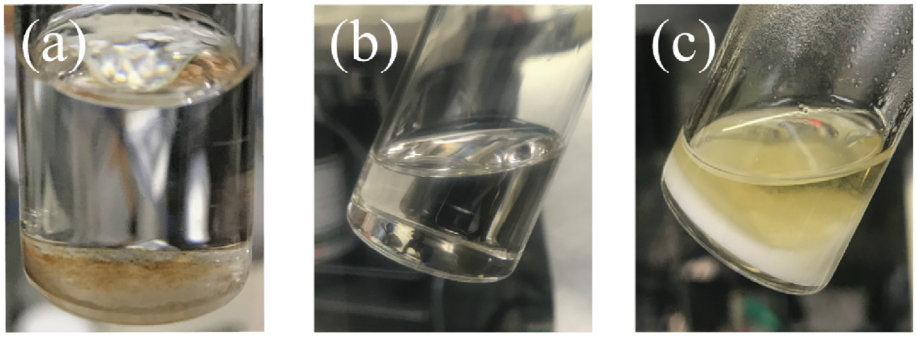

Fig. 1. Photographs of dissolution tests of $FeCl_2$ in (a) pure G2 and (b, c) $AlCl_3$–G2 solutions: (b) 0.025 mol dm^{-3} $FeCl_2$ and (c) excess $FeCl_2$.

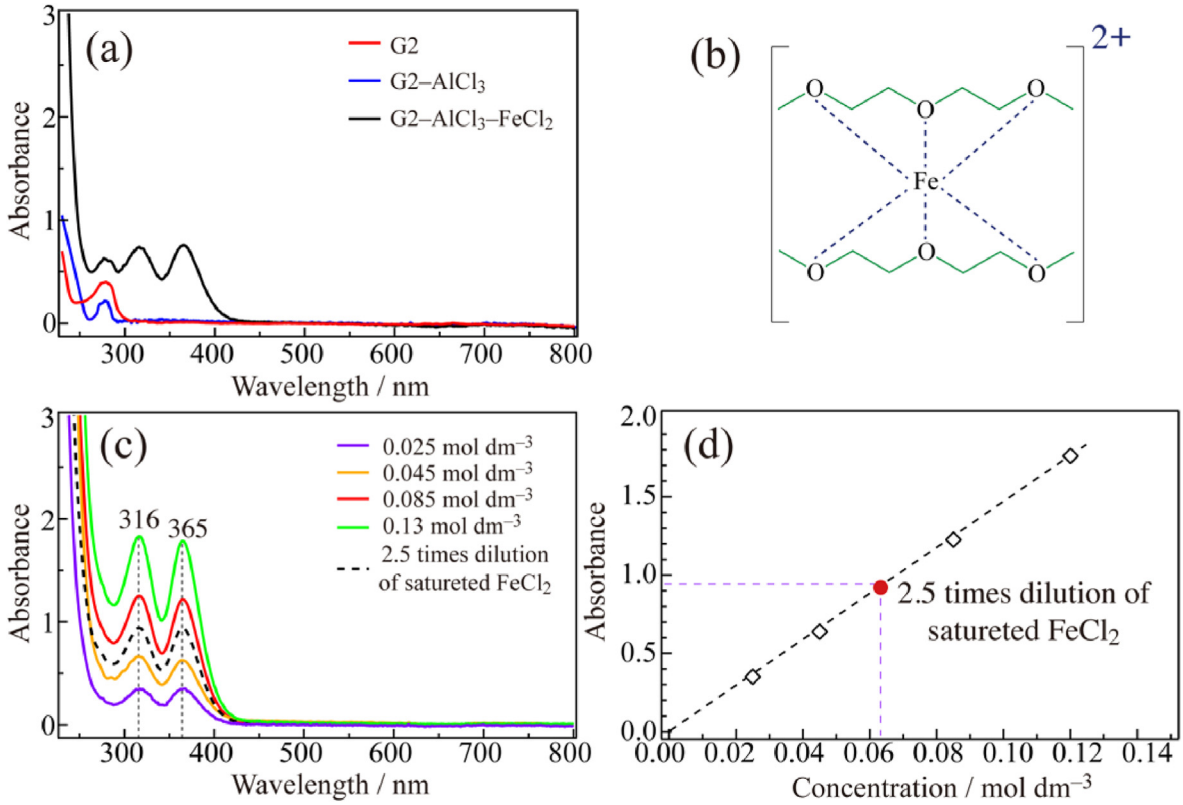

Fig. 2. (a) UV–Vis spectra of pure G2, $AlCl_3$–G2 and $FeCl_2$–$AlCl_3$–G2 solutions, (b) schematic structure of iron(II)–G2 complex, (c) spectra of $FeCl_2$–$AlCl_3$–G2 with different $FeCl_2$ concentrations and (d) plots of absorbance at 316 nm vs. $FeCl_2$ concentration in $AlCl_3$–G2 solution.

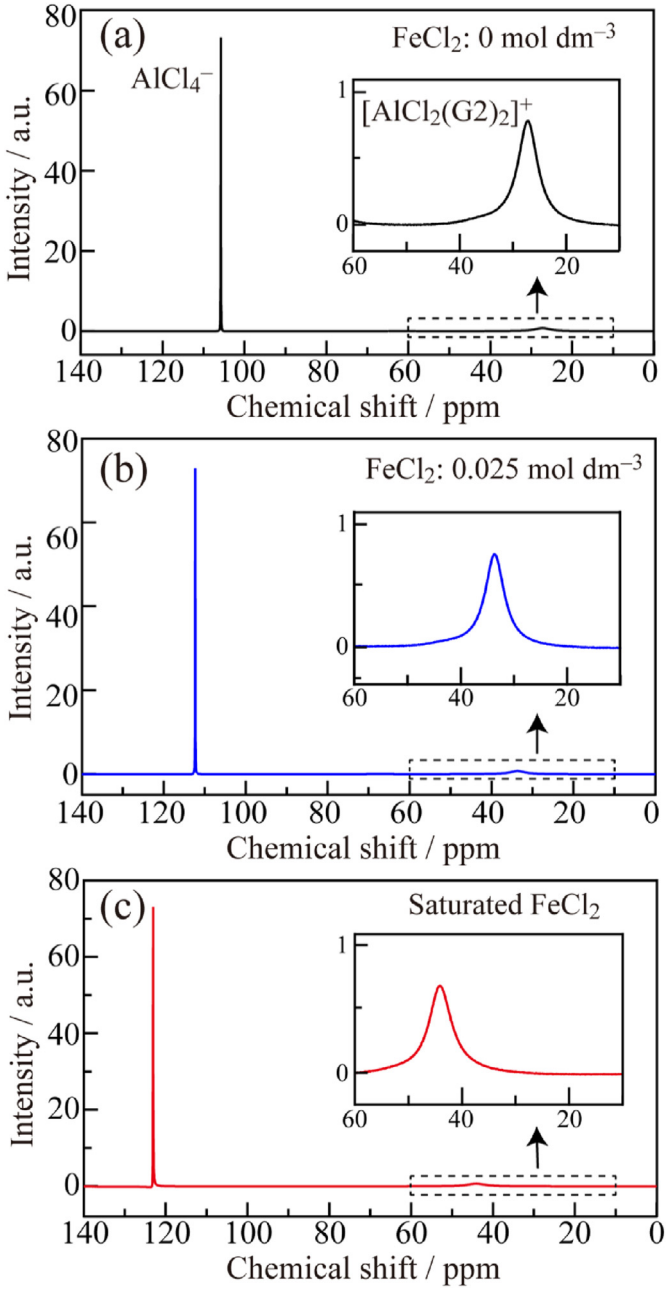

Fig. 3. ^{27}Al NMR spectra for $AlCl_3$–G2, $FeCl_2$–$AlCl_3$–G2 solutions with 0.025 mol dm^{-3} $FeCl_2$ and saturated $FeCl_2$ concentrations. Insets show the enlarged spectra between 60 and 10 ppm.

Co.). The ionic conductivities of the electrolytes were measured using electrochemical impedance spectroscopy in a temperature chamber (Espec Co., SU-222) with a self-made two-stainless-steel-electrode cell, and the cell constant was calibrated with a 0.1 mol dm^{-3} KCl aqueous solution. ^{27}Al nuclear magnetic resonance (NMR) spectra were obtained (200 scans; acquisition time, 1.5 s) by an NMR spectrometer at 600 MHz (JNM-ECA 600) referenced to DMSO-d_6 (99.9 at% D, Sigma-Aldrich). UV–Vis spectroscopy (Hitachi U-3500) was performed at a scan rate of 30 nm s^{-1} in 1-mm quartz cuvettes over the wavelength range of 200–800 nm. Raman spectroscopy was conducted using an InnoRam 785 (B&W Tek) equipped with a 785-nm semiconductor laser light source.

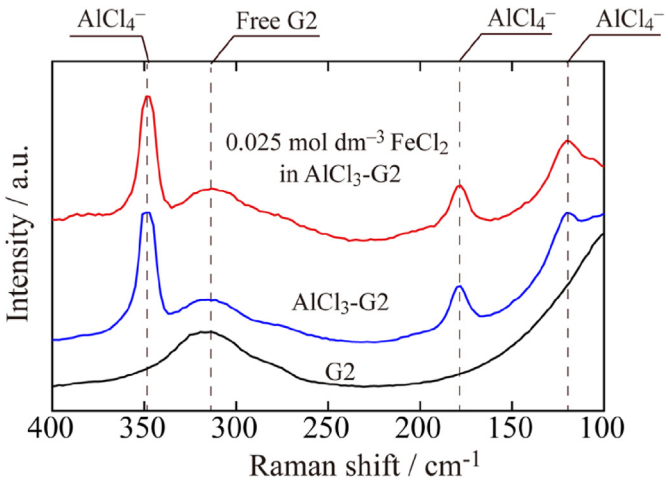

Fig. 4. Raman spectra of pure G2, $AlCl_3$–G2 and $FeCl_2$–$AlCl_3$–G2 solutions.

2.3. Electrochemical measurements and deposition

Cyclic voltammetry and potentiostatic electrodeposition were carried out with an electrochemical working station (Bio-Logic Science Instruments SAS, VSP-300). In the $FeCl_2$–G2–$AlCl_3$ baths, the three-electrode system consisted of a working electrode (Cu sheet, 2.0 × 0.5 cm), counter electrode (Fe sheet, 2.0 × 2.0 cm), and quasi-reference electrode (QRE, Fe sheet, 2.0 × 0.5 cm). Electrodeposition was conducted at different constant potentials. In the aqueous baths, Cu, Pt, and Hg/Hg_2SO_4 (ALS Co., Ltd.) were used as the working electrode, counter electrode, and the reference electrode (0.657 V vs. SHE), respectively. The cathodic electrodeposition in $FeCl_2$ aqueous electrolytes was conducted at a constant current density of 5 mA cm^{-2}, pH 3.0, and room temperature with a stirring speed of 500 rpm, which is the common condition for the Fe electrodeposition from aqueous solutions [8,13].

2.4. Characterization of deposits

The surface morphology of the deposit was characterized by a scanning electron microscope (SEM, Keyence VE-7800), and an X-ray diffraction (Rigaku RINT2200, Cu Kα) experiment was performed at a scan rate of 0.3° min^{-1}. A transmission electron microscope (TEM, JEM-2100F) equipped with an energy dispersive X-ray spectrometer (EDX, JED-2300T) was used for high-resolution transmission electron microscopy (HRTEM) observations, corresponding selected area electron diffraction (SAED), and chemical composition analysis. The samples for TEM and HRTEM were prepared by a focused ion beam (FIB, JEOL JFIB-2300) system.

3. Results and discussion

3.1. Solubility of $FeCl_2$

The solubility of the $FeCl_2$ in pure G2 and $AlCl_3$–G2 solution with a molar ratio of $AlCl_3$:G2 = 1:5 was investigated at 25 °C. Fig. 1(a) shows that the brown $FeCl_2$ powder in pure G2 remained undissolved. This insolubility of $FeCl_2$ in pure G2 can be explained by the strong Coulomb interaction between Fe^{2+} and Cl^-, which is not affected by ion–dipole interactions between Fe^{2+} and G2. By contrast, a pale green solution, as shown in Fig. 1(b), was obtained by adding small amounts of $FeCl_2$ into the $AlCl_3$–G2 solution. Prior to the tests, the $AlCl_3$–G2 solution was purified to be colorless through pre-electrolysis. As shown in Fig. 1(c), a higher molar ratio

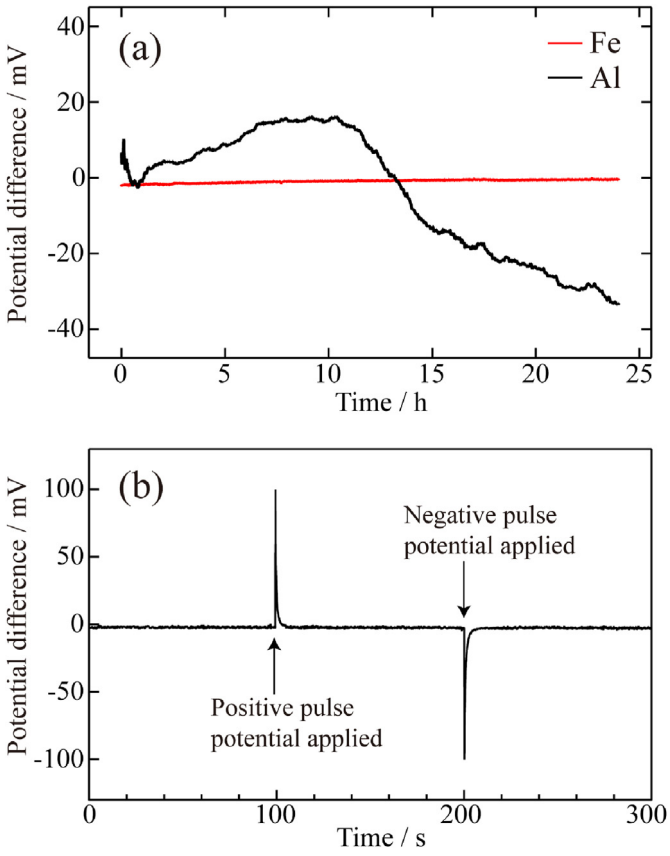

Fig. 5. (a) Time dependence of potential difference between two Fe electrodes and two Al electrodes immersed in $FeCl_2$–$AlCl_3$-G2 electrolyte with 0.025 mol dm^{-3} $FeCl_2$, and (b) time dependence of potential difference between two Fe electrodes immersed in $FeCl_2$–$AlCl_3$-G2 electrolyte with 0.025 mol dm^{-3} $FeCl_2$ when potential pulses of +100 and −100 mV vs. Fe QRE were applied at times of 100 and 200 s, respectively.

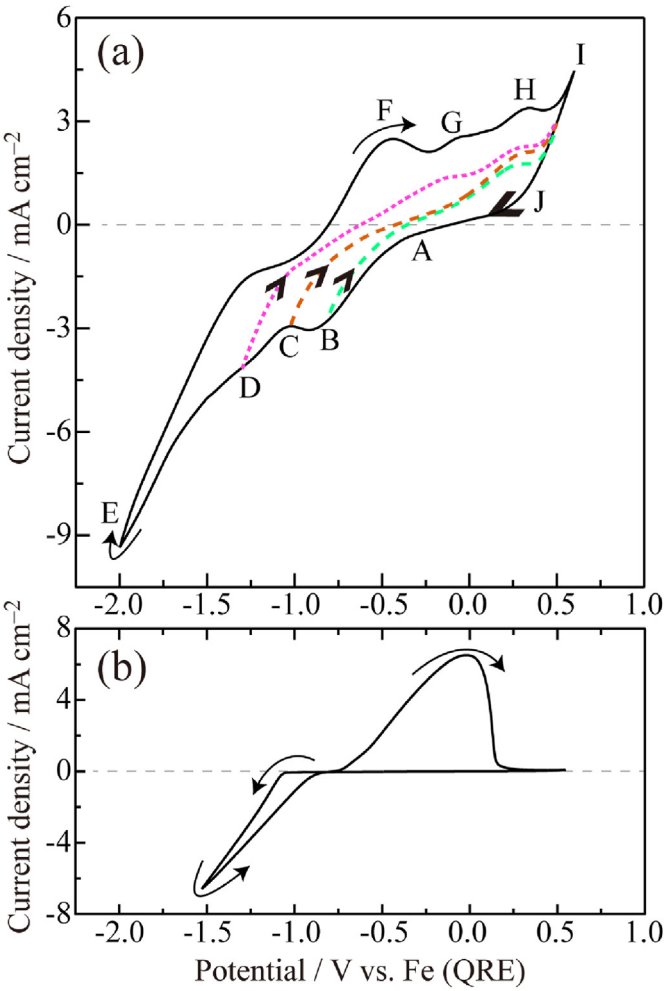

Fig. 6. Typical CVs for (a) 0.025 mol dm^{-3} $FeCl_2$ in $AlCl_3$–G2 electrolyte with different switching potentials at points B–E and (b) $AlCl_3$–G2 electrolyte. Sweep rate 20 mV s^{-1}.

of $FeCl_2$ led to a saturation with a pale-yellow color. Such limited solubility of $FeCl_2$ in Lewis acidic solutions has been reported for Lewis acidic chloroaluminate ionic liquids [23,24].

3.2. UV–Vis spectroscopy

UV–Vis spectroscopy was employed to investigate the speciation of the soluble $FeCl_2$ formed in the $AlCl_3$–G2 solution. In Fig. 2(a), baseline correction was carried out using an empty cell; hence, the spectrum obtained from the $FeCl_2$–$AlCl_3$–G2 solution was compared with the spectra of pure G2 and $AlCl_3$–G2 solution. The high-intensity bands between 300 and 400 nm arose from electronic transitions in the formed iron(II) complex. Each peak at 316 and 365 nm contributes to the ligand-centered band and metal-to-ligand charge transfer transition, respectively [25–27]. These peaks are similar to those for [bis-tpy]Fe(II) formed in 2,2′:6′,2″-terpyridine (tpy) with dissolved $FeCl_2$ [27,28]. In addition, a metal–glyme complex $[Mg(G1)_3]^{2+}$ appears in $MgCl_2$–$AlCl_3$–G1 (G1: monoglyme or 1,2-dimethoxyethane) when the amount of $MgCl_2$ is less than equimolar $AlCl_3$ [29]. Therefore, it was considered that an oxygen ligand was attached to the Fe, forming a [bis-G2]Fe(II) complex ($[Fe(G2)_2]^{2+}$), as shown in Fig. 2(b). The possibility of an iron–chloride–diglyme complex $[FeCl(G2)_n]^{+}$ is low, because the excess $AlCl_3$ may lead to a chloride abstraction from $[FeCl(G2)_n]^{+}$ to form $[Fe(G2)_2]^{2+}$ and $AlCl_4^-$, as in $MgCl_2$–$AlCl_3$–G1 [29].

In Fig. 2(c) and (d), baseline correction was carried out using $AlCl_3$–G2 solution. The absorbance of each sample increased linearly with the concentration of $FeCl_2$. The relationship between the absorbance and the concentration was used to estimate the saturated concentration. The maximum solubility of $FeCl_2$ in $AlCl_3$–G2 solution with a molar ratio of 1:5 was approximately 0.15 mol dm^{-3}.

3.3. ^{27}Al NMR and Raman spectroscopy

^{27}Al NMR spectroscopy was performed to check the influence of the $FeCl_2$ addition on Al complexes in the G2 electrolytes. As shown in Fig. 3, each spectrum for $AlCl_3$–G2 and $FeCl_2$–$AlCl_3$–G2 solutions has a sharp peak at high frequencies corresponding to an $AlCl_4^-$ anion and a broad peak with lower intensity resulting from an $[AlCl_2(G2)_2]^{+}$ cation [30,31]. The chemical shifts of $\delta(^{27}Al)$ for $AlCl_4^-$ and $[AlCl_2(G2)_2]^{+}$ move downfield along with the increase in the amount of $FeCl_2$. The observed downfield shift indicates that the ferrous ions decreased the electron density around the Al by attractive interaction between $[Fe(G2)_2]^{2+}$ and $AlCl_4^-$ and by decreasing the amount or activity of G2 in $[AlCl_2(G2)_2]^{+}$. The ratio of the peak area for $[AlCl_2(G2)_2]^{+}$ to that for $AlCl_4^-$ decreases with increasing $FeCl_2$ content, providing evidence that $FeCl_2$ reacts with $[AlCl_2(G2)_2]^{+}$ to form $AlCl_4^-$. Therefore, the Fe^{2+}–G2 complex forms with the help of $AlCl_3$, which is consistent with the UV–Vis results.

$FeCl_2$ dissolved into Lewis basic chloride baths could exist as a

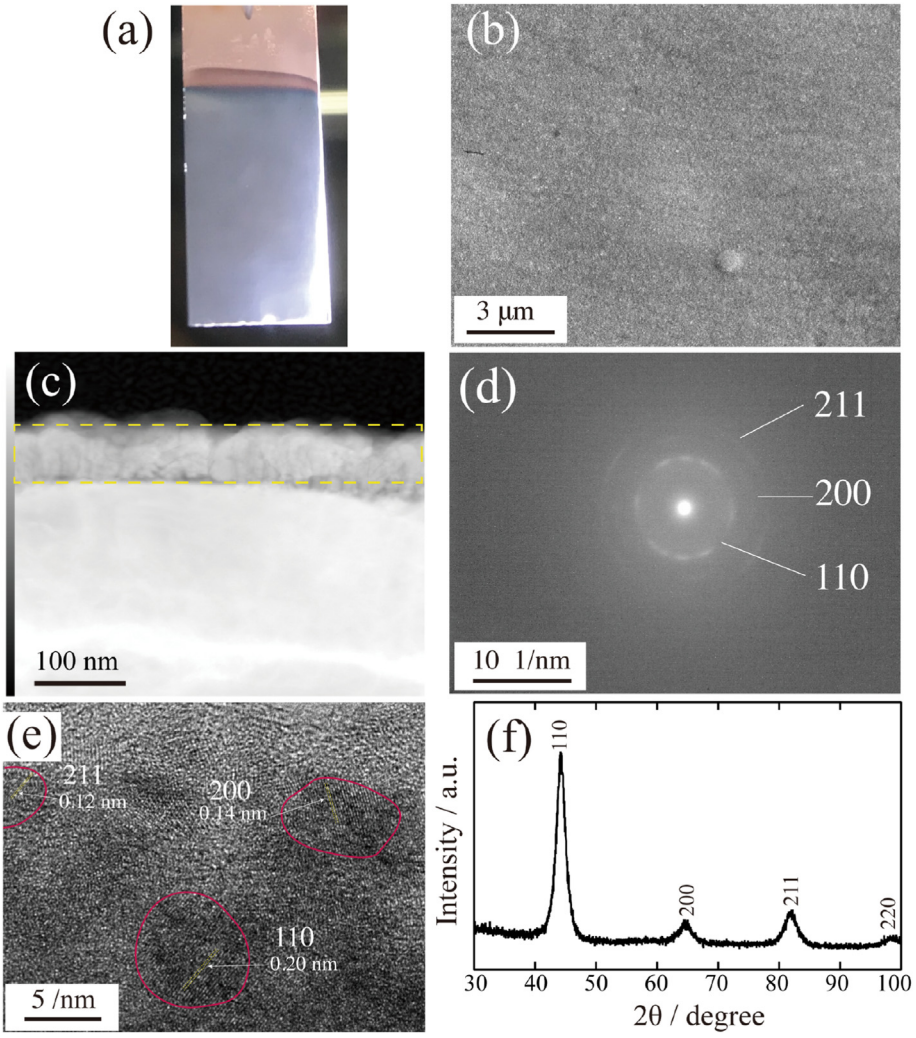

Fig. 7. (a) Photograph, (b) plan view SEM image, (c) cross-sectional view dark-field image, (d) SAED pattern, (e) HRTEM image and (f) XRD profile of the Fe sample electrodeposited at −0.5 V vs. Fe QRE.

$FeCl_4^{2-}$ anion [20,32]. However, the Raman spectra of $FeCl_2$–$AlCl_3$–G2 solution shown in Fig. 4 does not correlate well with that for $FeCl_4^{2-}$ with a characteristic peak at 265 cm^{-1} [32]. In addition, the spectrum of $AlCl_4^-$ formed in $AlCl_3$–G2 and $FeCl_2$–$AlCl_3$–G2 solutions presents the same feature. This indicates a weak correlation between $AlCl_4^-$ and Fe(II), which is also reported in the Lewis neutral haloaluminate ionic liquids [23,24].

Therefore, the reactions between $FeCl_2$ and $AlCl_3$–G2 solution can be represented by the following equations:

$$2AlCl_3 + 2G2 \rightleftharpoons [AlCl_2(G2)_2]^+ + AlCl_4^- \quad (1)$$

$$FeCl_2 + [AlCl_2(G2)_2]^+ \rightleftharpoons [Fe(G2)_2]^{2+} + AlCl_4^- \quad (2)$$

In Eq. (1), $AlCl_3$ reacts with G2 to form a hexacoordinate $[AlCl_2(G2)_2]^+$ complex cation and $AlCl_4^-$ anion. As a result of the UV–Vis, ^{27}Al NMR, and Raman spectrum analysis, Eq. (2) is proposed — the reaction between $FeCl_2$ and $[AlCl_2(G2)_2]^+$ to form $[Fe(G2)_2]^{2+}$. By contrast, $FeCl_4^-$ is known to be formed in haloaluminate ionic liquids, such as $AlCl_3$–BPC (*N*-*n*-butylpyridinium chloride) acidic or basic ionic liquids, and the neutral $AlCl_3$–BPC bath fails to dissolve the $FeCl_2$ [24]. $Al_2Cl_7^-$ in acidic ionic liquid or excess Cl^- in basic ionic liquid is responsible for the formation of Fe–Cl complex $FeCl_4^{2-}$. In $AlCl_3$–G2 solution, $[AlCl_2(G2)_2]^+$ exists instead of $Al_2Cl_7^-$ and Cl^-. Therefore, the reaction between $[AlCl_2(G2)_2]^+$ and ferrous ion gives $[Fe(G2)_2]^{2+}$.

3.4. Cyclic voltammetry and potentiostatic electrodeposition

In general, Al can be employed as a QRE in $AlCl_3$-containing electrolytes for subsequent measurement of cyclic voltammetry and potentiostatic electrodeposition [33–37]. However, when Al was used as QRE in the $FeCl_2$–$AlCl_3$–G2 electrolyte, the potential difference between two Al electrodes fluctuated considerably (Fig. 5(a)). This is because a displacement reaction occurred between Al metal and Fe^{2+} to give Al^{3+} and Fe metal, and the potential-determining reaction cannot be unique. Here, the feasibility of Fe as a 'reference electrode of the first kind' in $FeCl_2$–$AlCl_3$–G2 electrolyte was examined, by referring a previous report of Sn electrode in an ionic liquid electrolyte [38]. First, the potential difference between two Fe electrodes was measured, proving that the Fe electrode possesses a long-term stability within 1 mV (Fig. 5(a)). A further experiment was carried out using a couple of Fe electrodes immersed in $FeCl_2$–$AlCl_3$–G2 electrolyte. As shown in Fig. 5(b), after applying potential pulses of +100 and −100 mV vs. Fe electrode, the potential difference returned to

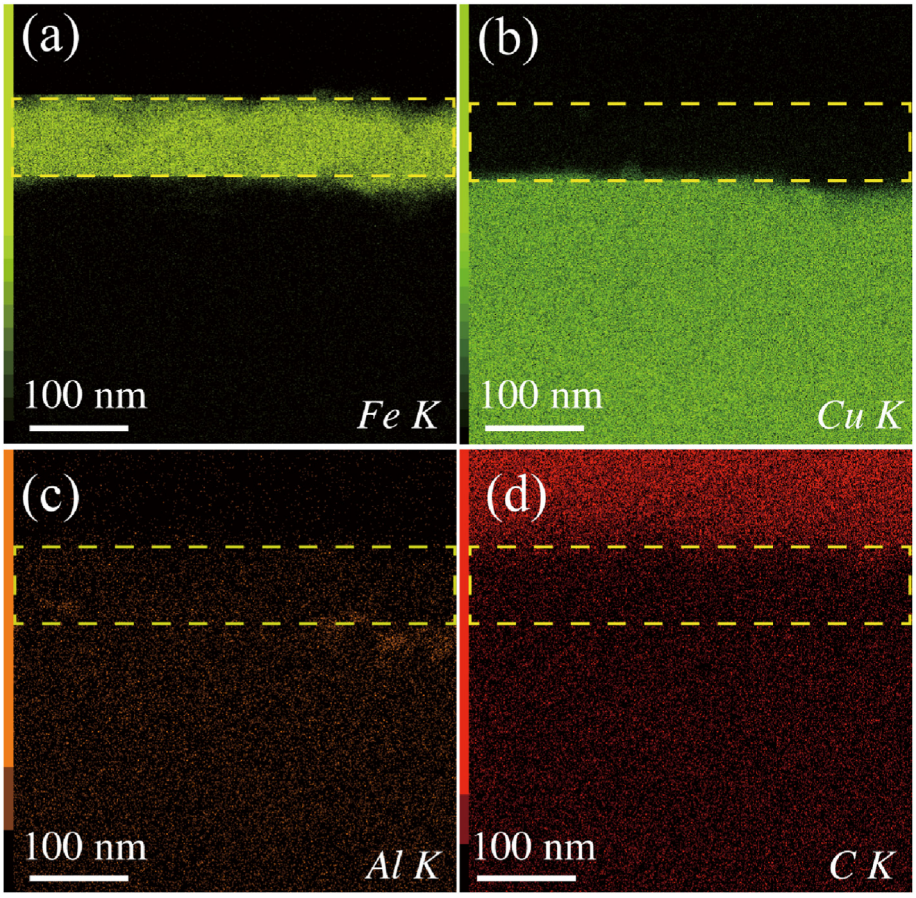

Fig. 8. EDX mapping of the Fe sample electrodeposited at −0.5 V vs. Fe QRE.

the original value within a few seconds, substantiating that the immersion potential of Fe electrodes is stable against external electrical disturbance as is always required for a reference electrode. Therefore, Fe can be employed as a QRE in this system. A half reaction should be written as $[Fe(G2)]^{2+} + 2e \rightleftharpoons Fe + 2G2$.

Fig. 6(a) displays cyclic voltammograms (CVs) with varying switching potentials at points B, C and D for the $FeCl_2$–$AlCl_3$–G2 electrolyte with 0.025 mol dm^{-3} $FeCl_2$. The CVs differ from those of the $AlCl_3$–G2 electrolyte, as shown in Fig. 6(b), indicating that Fe electrodeposition has occurred. As for the $FeCl_2$–$AlCl_3$–G2 electrolyte, the scan starts from open-circuit voltage toward the negative direction, and the redox couple HI/IJ refers to Cu oxidation [36]. The reduction to Fe starts from point A, as described below. The iron–diglyme complex $[Fe(G2)_2]^{2+}$ indicated by Eq. (2) should be an active species for the reduction to Fe. The following reduction wave BC is also attributed to Fe electrodeposition. This assignment is supported by the fact that the reduction onset AB and a plateau BC correspond to an almost identical oxidation process. The reduction wave BC reaches a plateau at 3.2 mA cm^{-2}, because the system is in a diffusion-limited condition.

A constant potential −0.5 V vs. Fe QRE was applied for cathodic electrodeposition. Fig. 7(a) shows that the Cu substrate was covered by a deposit that was bright. The brightness originates from a void-free and smooth surface, as displayed by the SEM image in Fig. 7(b). TEM observations and electron diffraction measurements — see Figs. 7(c)–(e) — show that the deposit was composed of pure Fe with a body-centered cubic (bcc) structure, and the size of the crystallite, marked by magenta circles, was approximately 10 nm. This is consistent with the results of CV, as shown in Fig. 6(a). An XRD profile with broadened peaks is shown in Fig. 7(f), and it confirms that the deposition film, peeled from the copper substrate, was composed of crystalline α-Fe. Additionally, the average crystallite size was estimated to be 10 nm by Scherrer's equation [39], which is consistent with the TEM result in Fig. 7(e). The smaller Fe crystallite size contributes to a smooth surface. The observed lattice distances shown in Fig. 7(e) are consistent with the unit cell size of α-Fe (0.287 nm), suggesting that the nanocrystals exhibit high purity. The absence of Al and C impurities is supported by the EDX mappings shown in Fig. 8, suggesting that Al^{3+}–glyme complexes are not reduced at −0.5 V vs. Fe QRE. A potentiostatic electrodeposition at −0.6 V vs. Fe QRE successfully gave a bright Fe thin film, as in the case at −0.5 V. It is emphasized that such a bright and compact Fe thin film is extremely difficult to obtain from aqueous baths [13]. In previous studies on nonaqueous baths, only non-compact deposits of Fe nanoparticles, rather than film morphology, have been obtained in choline chloride (ChCl)–urea deep eutectic solvent with dissolved Fe(III) [17] and $AlCl_3$–1-methyl-3-butylimidazolium chloride ionic liquid with dissolved Fe(II) [18].

Without $FeCl_2$, metallic Al can be produced from the $AlCl_3$–G2 bath — see Fig. 6(b). In the CVs shown in Fig. 6(a) from point C to point E, there is a steep increase of current density. The standard redox potential of Al/Al^{3+} is −1.67 V vs. SHE, which can be converted to approximately −1.2 V vs. Fe QRE — see Fig. 6(b). As the transition stage at D is around −1.2 V, the CVs shown in Fig. 6(a) gave faradaic current densities similar to that of $AlCl_3$–G2 electrolyte (Fig. 6(b)). It is speculated that the electrodeposition of Fe–Al alloys and pure Al and may occur below approximately −1.2 V vs. Fe QRE. New oxidation peaks at points F

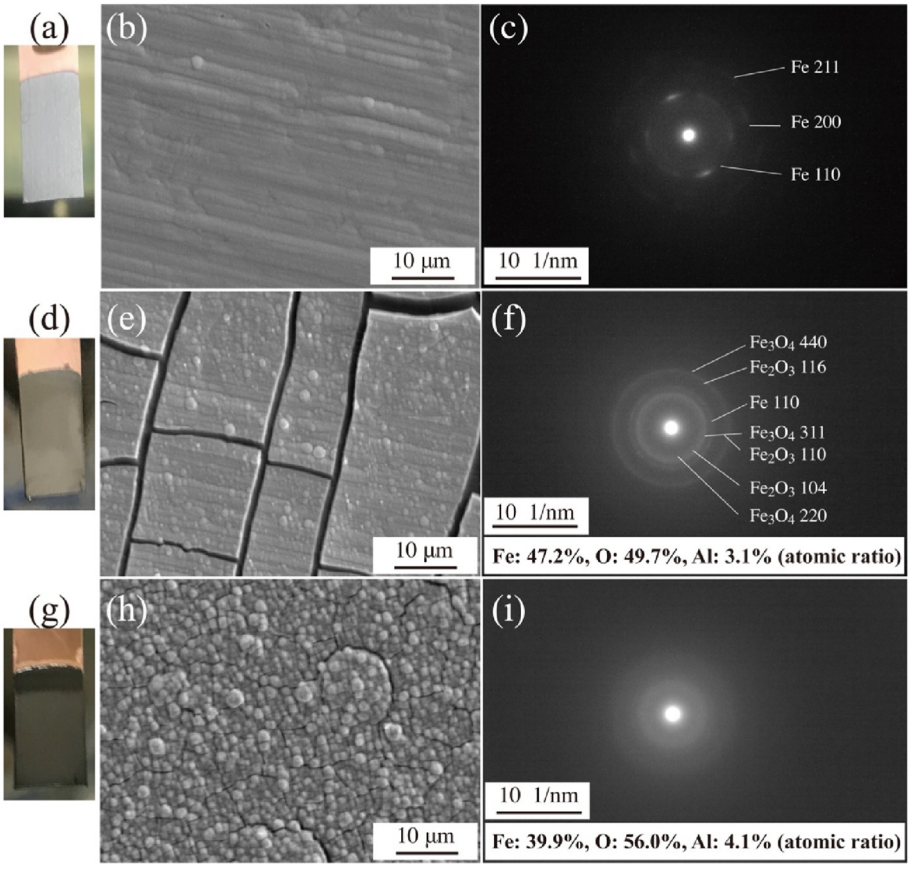

Fig. 9. Photographs, plan view SEM images and SAED patterns of samples deposited at different potentials of (a)–(c) −1.0 V, (d)–(f) −1.5 V, and (g)–(i) −2.0 V vs. Fe QRE; TEM-EDX results are provided in (f) and (i).

and G appear below 0 V vs. Fe QRE. Since the oxidation wave at point F is absent for the voltammogram switched at point D (dashed pink curve in Fig. 6(a)), points F and G is considered to be dissolution of electrodeposited pure Al and Fe–Al alloys, respectively.

A set of potentiostatic electrodeposition at more-negative potentials was conducted. In Figs. 9(a)–(c), the compact deposits obtained at a potential of −1.0 V vs. Fe QRE are also pure Fe with a metallic luster. At potentials of −1.5 V (Figs. 9(d)–(f)), the TEM-EDX results (Fig. 9(f)) revealed that the deposits contained Fe, O and Al. To obtain average information of the whole deposits, XRD measurements were conducted at the same condition as the case of −0.5 V. In Fig. S1 (ESI†), Fe and Fe oxides were observed, consistent with the SAED results shown in Fig. 9(f). At more negative potentials of −2.0 V (Figs. 9(g)–(i)), the SAED and TEM-EDX results shown in Fig. 9(i) revealed that the deposits had a much lower crystallinity and also contained Fe, O and Al. Therefore, only metallic Fe with low intensity was observed in Fig. S1 (ESI†) and the XRD peaks of Fe oxides and the possible Al/Al oxide phases should be hidden in the background. Deposits obtained at −1.5 V and −2.0 V had many cracks, and these larger specific surface areas resulted in rapid oxidation in air to give Fe oxides as a main phase.

There were no diffraction peaks of metallic Al or Al oxides for the whole deposits (Fig. S1, ESI†). In general, contaminants with their contents less than a few percentage are not detectable by X-ray diffraction. This further confirmed that only a very small amount of Al existed in the deposits, supported by the TEM-EDX results (Figs. 9(f) and (i)). However, it seems contradictory to what is predicted by the CVs shown in Fig. 6(a), where reduction of Al^{3+} was observed at −1.5 V and −2.0 V in the short-term electrolysis. In the case of long-term electrodeposition, however, Fe^{2+} reduction became dominant even though the $FeCl_2$ concentration was two orders of magnitude lower than $AlCl_3$ and the applied potentials were fairly negative. We speculate that the Cu surface still appeared during a short-term electrolysis like CVs and Al^{3+} reduction on Cu may take place, while for a long-term electrolysis Cu was totally covered with Fe deposits and the Al^{3+} reduction became hard to occur. Therefore, the reduction rate of Fe^{2+} should be higher than that of Al^{3+} for the long-term electrolysis. Besides, according to Nernst equation, Fe^{2+}/Fe still had a more positive reduction potential than Al^{3+}/Al in $FeCl_2$–$AlCl_3$–G2 electrolyte with $FeCl_2$ of 0.025 mol dm^{-3}. Therefore, the driving force for Fe^{2+} reduction became larger at more negative potentials and the bulk concentration of $FeCl_2$ (0.025 mol dm^{-3}) was not so dilute.

The results should also be considered from the viewpoint of the iron impurity effect on Al electrodeposition. Iron is the major impurity in $AlCl_3$ [40]. Recently, $AlCl_3$–organic baths have attracted attention for plating and batteries [41]. There have been reported other $AlCl_3$-containing organic baths [33,42,43], where cationic complexes $[AlCl_2(ligand)_n]^+$ similar to $[AlCl_2(G2)_2]^+$. Based on the results of $FeCl_2$–$AlCl_3$–G2 electrolyte, it can be deduced that the rate of Al^{3+} reduction could also be much lower if $FeCl_2$ contaminates the baths and reacts with the cationic complexes $[AlCl_2(ligand)_n]^+$ to form $[Fe(ligand)_n]^{2+}$. Therefore, even a very small amount of iron impurity in the electrolyte prevents the Al electrodeposition and influences the properties of batteries.

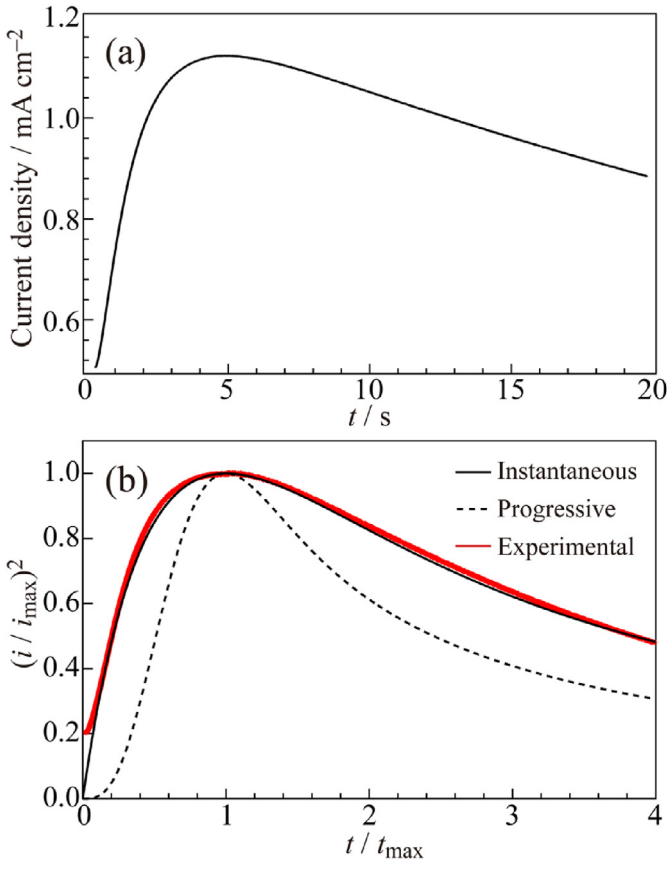

Fig. 10. (a) Current–time transient for the potentiostatic electrodeposition at −0.5 V vs. Fe QRE and (b) the corresponding $(i/i_{max})^2$-t/t_{max} plot and the theoretical models for instantaneous and progressive nucleation.

3.5. Current–time transient of Fe electrodeposition for the G2 electrolyte

Fig. 10(a) shows the typical current–time transient for the electrodeposition of Fe at a potential of −0.5 V vs. Fe QRE. The current density increased initially with time and reached a maximum i_{max} for the nucleation and growth of Fe particles. Then, the current–time transient was followed by a decrease resulting from a diffusional overlap. The Scharifker–Hills (S–H) models were used to analyze the current–time transient, to distinguish between the instantaneous nucleation mechanism and the progressive one [44]. In instantaneous nucleation, all the sites for nucleation are activated at the same time, and the nuclei grow at the same rate. In progressive nucleation, the nuclei are still produced along with their growth, and the ages of the nuclei are different. The processes of instantaneous and progressive nucleation, as in Fig. 10(b), can be expressed as Eqs. (3) and (4), respectively:

$$\frac{i^2}{i_m^2} = \frac{1.9542}{\frac{t}{t_m}}\left\{1-\exp\left[-1.2564\left(\frac{t}{t_m}\right)\right]\right\}^2 \quad (3)$$

$$\frac{i^2}{i_m^2} = \frac{1.2254}{\frac{t}{t_m}}\left\{1-\exp\left[-2.3367\left(\frac{t}{t_m}\right)^2\right]\right\}^2 \quad (4)$$

The experimental current–time transient can be replotted as in Fig. 10(b) and compared with the S–H models. As a result, the potentiostatic electrodeposition at −0.5 V can be understood by the model of the instantaneous nucleation mechanism. Hence, the reason why the Fe deposits present a compact and smooth surface is not only because there is no interference from H_2 gas evolution and the additives. By contrast, previously-reported electrodeposition from nonaqueous solutions are based on progressive nucleation, failed to obtain a compact and smooth films [19,20].

The S–H models can provide an estimate of the nucleation number density of active sites N_0. For the three-dimensional instantaneous nucleation process, the value of N_0 can be estimated from the values of i_{max} and t_{max} in by the following equations [45]:

$$N_0 = 0.065\left(\frac{nFC}{i_{max}t_{max}}\right)^2 \Big/ (8\pi CM/\rho)^{1/2} \quad (5)$$

where n is the number of electrons transferred for each Fe atom deposited, F is Faraday constant, C is concentration of Fe^{2+}, M and ρ are molar weight and density of Fe. There have been several literatures where N_0 is estimated using Eq. (5) [46,47]. However, the previous studies showed that the considerable discrepancies exist in the values of N_0 between that estimated from Eq. (5) and that estimated by counting particles on SEM images deposited for a short time, e.g. t_{max}. The reported values of N_0 are as large as 10^{13}–10^{16} cm^{-2} at t_{max}, a several orders of magnitude larger than those estimated from Eq. (5). Moreover, for the previous studies, aggregation of particles occurred before t_{max} [46,47]. This strongly suggests that the preposition of the S–H model, i.e. the assumption of three-dimensional diffusion controlled growth of the nuclei, is not satisfied for the previous studies.

In our case, however, the discrepancy is rather small and no aggregation was observed at t_{max}, evidencing the utility of S–H models in our case. For the potentiostatic electrodeposition at −0.5 V, the calculated value of N_0 using Eq. (5) is 1.13×10^6 cm^{-2}. Fig. 11(a) is the SEM image of the Fe deposits obtained by potentiostatic electrodeposition at −0.5 V for $t_{max} = 4$ s. The value of N_0, calculated by counting the particles in Fig. 11(a), was about 1.5×10^7 cm^{-2}. Although this is about ten times higher than N_0 obtained using Eq. (5), it is more important that the individual Fe nuclei are isolated from one another and distributed on the Cu substrate at $t = t_{max} = 4$ s (Fig. 11(a)). Even at $t = 30$ s, the nuclei became larger with the similar particle densities (Fig. 11(b)), proving that the preposition of the S–H model, i.e. the assumption of three-dimensional diffusion controlled growth of the nuclei, is satisfied. As a result, the deviation is ignorable between the fitting and the experimental curves in Fig. 10(b), in stark contrast to the previous studies [46,47].

3.6. Comparison with aqueous electrolytes

Fig. S2 (ESI†) shows the CVs of the $FeCl_2$-based aqueous electrolytes with different concentrations. In Figs. S2(a) and (e), the electrolyte contains 0.025 mol dm^{-3} $FeCl_2$ — the same as that in the $FeCl_2$–G2–$AlCl_3$ electrolyte. There was a clear increase in current density when the potentials were swept to −0.87 and −1.07 V. Because the standard potential of Fe^{2+}/Fe^0 (−0.44 V vs. SHE) is more negative than that of the H_2 evolution reaction, the initial increase of current density in region I — see Figs. S2(e)–(h) — results from the H_2 evolution. Based on the Nernst equation, the estimated reduction potential of H^+/H_2 in these aqueous electrolytes with pH = 3 is −0.09 V, which is consistent with the potential initiating the increase of the current density in the CVs — see Figs. S2(e)–(h). Then, there was a sudden increase in the current density in region II, as shown in Figs. S2(e)–(h), indicating the electrodeposition of metallic Fe. The increased concentration of $FeCl_2$ enhanced the current density in the CVs, as shown in

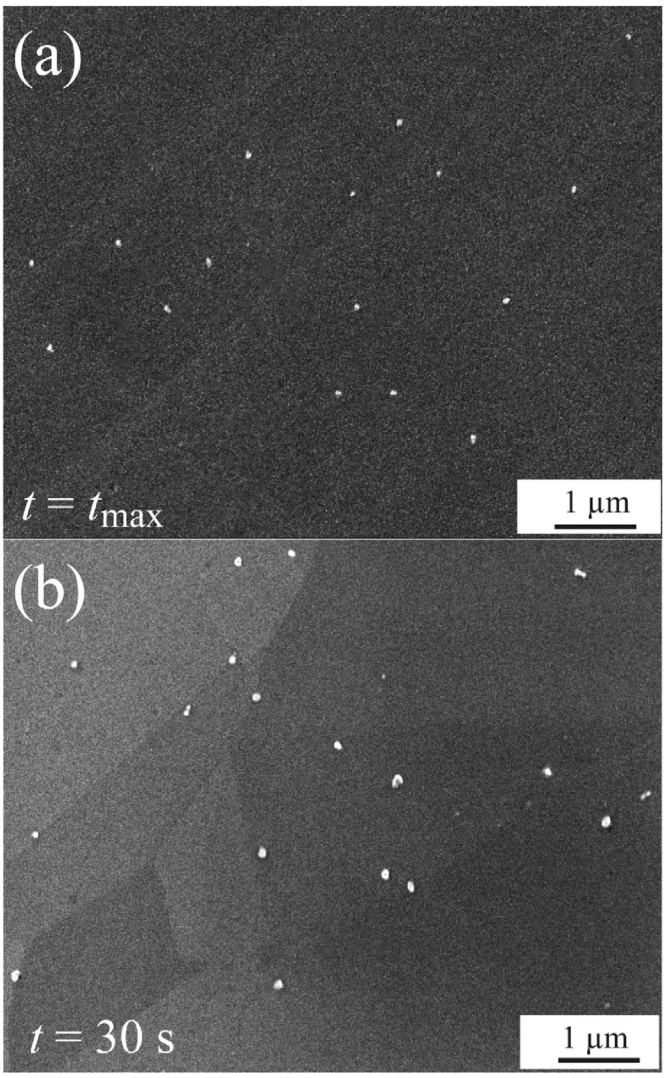

Fig. 11. SEM images of the Fe deposits electrodeposited at −0.5 V vs. Fe QRE for (a) $t = t_{max} = 4$ s and (b) $t = 30$ s.

Figs. S2(a)–(d); meanwhile, the current density for Fe deposits decreased because of H_2 evolution and overpotential — see Figs. S2(e)–(h). The peaks between 0 and + 0.2 V in Figs. S2(b)–(d) were the result of Cu oxidation.

Figs. S3(a)–(f) (ESI†) show that the Fe deposits had a metallic luster and were scattered with voids, where the reduced H_2 adhered to Fe deposits during electrodeposition. With additives, however, the samples showed a black appearance, as shown in Fig. S3(h), and granular microstructure — see Fig. S3(g). Therefore, H_2 gas evolution and the additives in aqueous electrolytes interfere with the growth of deposits, and subsequently lead to a non-compact and rough surface morphology. Instead of aqueous electrolytes, Fe can be deposited uniformly from nonaqueous $FeCl_2$–$AlCl_3$–G2 electrolyte without H_2 gas evolution, resulting in a compact and smooth Fe thin film.

4. Conclusions

A nonaqueous electrolyte, $FeCl_2$–$AlCl_3$–G2, made the electrodeposition of Fe thin film successful. Electrodeposition at a constant potential of −0.5 V vs. Fe QRE gave a compact structure and smooth surface, not only because the Fe nucleates in an instantaneous nucleation mechanism, but also because the influence of H_2 gas evolution was excluded. The obtained Fe deposits were composed of nanocrystals, the grain size of which was much smaller than those in previous reports. This burnished Fe film has potential applications in high-precision optical devices [48], as well as electromagnetic devices. Related studies are planned for the future. $FeCl_2$ cannot be dissolved into G2 without the help of $AlCl_3$, and the electrochemically active species should be the $[Fe(G2)_2]^{2+}$ cation. Moreover, this study has shown the possibility that the properties of Al-ion batteries and Al plating baths could be significantly degraded by a very small amount of iron “impurity”.

CRediT authorship contribution statement

Zelei Zhang: Validation, Formal analysis, Investigation, Data curation, Writing - original draft, Visualization, Funding acquisition. **Atsushi Kitada:** Conceptualization, Methodology, Data curation, Writing - review & editing, Visualization, Supervision, Project administration, Funding acquisition. **Kazuhiro Fukami:** Writing - review & editing, Visualization. **Zhengjun Yao:** Visualization, Funding acquisition. **Kuniaki Murase:** Writing - review & editing, Visualization.

Acknowledgments

We would like to thank Mr. N. Sasaki, Mr. K. Kazumi, and Mr. M. Saimura for their help in TEM and NMR experiments. This work is funded by Grants-in-Aid for Scientific Research (B) (No. 19H02490: A. K.) from the Japan Society for the Promotion of Science (JSPS), Iketani Science and Technology Foundation (No. 0311028-A), Open Fund of Key Laboratory of Material Preparation and Protection for Harsh Environment (Nanjing University of Aeronautics and Astronautics, No. 56XCA17006-3), and China Scholarship Council (CSC, No. 201806830035). The authors declare no competing interests.

Appendix A. Supplementary data

Supplementary data to this article can be found online at https://doi.org/10.1016/j.electacta.2020.136289.

References

[1] M. Mebarki, A. Layadi, M.R. Khelladi, A. Azizi, N. Tiercelin, V. Preobrazhensky, P. Pernod, Metall. Mater. Trans. A 47a (2016) 3677.
[2] D.D.L. Chung, J. Mater, Eng. Perform. 9 (2000) 350.
[3] J. Kemmer, S. Wilfert, J. Kügel, T. Mauerer, P.J. Hsu, M. Bode, Phys. Rev. B 91 (2015) 184412.
[4] M.N. Baibich, J.M. Broto, A. Fert, F.N. Vandau, F. Petroff, P. Eitenne, G. Creuzet, A. Friederich, J. Chazelas, Phys. Rev. Lett. 61 (1988) 2472.
[5] Y. Cao, K. Xu, W.L. Jiang, T. Droubay, P. Ramuhalli, D. Edwards, B.R. Johnson, J. McCloy, J. Magn, Magn. Mater. 395 (2015) 361.
[6] T. Kampfrath, R.G. Ulbrich, F. Leuenberger, M. Munzenberg, B. Sass, W. Felsch, Phys. Rev. B 65 (2002) 104429.
[7] K. Heusler, Electrochim. Acta 15 (1970) 243.
[8] S. Yoshimura, S. Yoshihara, T. Shirakashi, E. Sato, Electrochim. Acta 39 (1994) 589.
[9] E. Jartych, D. Chocyk, A. Budzynski, M. Jalochowski, Appl. Surf. Sci. 180 (2001) 246.
[10] J.A. Koza, M. Uhlemann, A. Gebert, L. Schultz, J. Electroanal, Chem. 617 (2008) 194.
[11] D. Grujicic, B. Pesic, Electrochim. Acta 50 (2005) 4405.
[12] E. Jartych, J.K. Zurawicz, E. Maczka, J. Borc, Mater. Chem. Phys. 72 (2001) 356.
[13] D. Kim, D.Y. Park, B.Y. Yoo, P.T.A. Sumodjo, N.V. Myung, Electrochim. Acta 48 (2003) 819.
[14] E. Jartych, M. Jalochowski, M. Budzynski, Appl. Surf. Sci. 193 (2002) 210.
[15] B. Koo, B. Yoo, Surf. Coating. Technol. 205 (2010) 740.
[16] V. Haehnel, S. Fähler, P. Schaaf, M. Miglierini, C. Mickel, L. Schultz, H. Schlörb, Acta Mater. 58 (2010) 2330.
[17] M. Palomar-Pardavé, J. Mostany, R. Muñoz-Rizo, L.E. Botello, J. Aldana-González, E.M. Arce-Estrada, M.G.M. de Oca-Yemha, M.T. Ramírez-Silva, M.R. Romo, J. Electroanal. Chem. 851 (2019) 113453.
[18] C.L. Aravinda, W. Freyland, Chem. Commun. (2004) 2754.

[19] T. Le Manh, E.M. Arce-Estrada, I. Mejia-Caballero, E. Rodriguez-Clemente, W. Sanchez, J. Aldana-Gonzalez, L. Lartundo-Rojas, M. Romero-Romo, M. Palomar-Pardave, J. Electrochem. Soc. 165 (2018). D808.
[20] M.A. Miller, J.S. Wainright, R.F. Savinell, A796, J. Electrochem. Soc. 164 (2017).
[21] H.Y. Huang, C.J. Su, C.L. Kao, P.Y. Chen, J. Electroanal. Chem. 650 (2010) 1.
[22] S.Y. Ha, Y.W. Lee, S.W. Woo, B. Koo, J.S. Kim, J. Cho, K.T. Lee, N.S. Choi, Acs Appl, Mater. Interfaces 6 (2014) 4063.
[23] D.P. Xue, Y. Yang, G.P. Ling, Green Energy Environ. 2 (2017) 412.
[24] T.M. Laher, C.L. Hussey, Inorg. Chem. 21 (1982) 4079.
[25] F. Messina, E. Pomarico, M. Silatani, E. Baranoff, M. Chergui, J. Phys, Chem. Lett. 6 (2015) 4475.
[26] S. Mukherjee, D.E. Torres, E. Jakubikova, Chem. Sci. 8 (2017) 8115.
[27] U. Mansfeld, M.D. Hager, R. Hoogenboom, C. Ott, A. Winter, U.S. Schubert, Chem. Commun. (2009) 3386.
[28] P.S. Braterman, J.I. Song, R.D. Peacock, Inorg. Chem. 31 (1992) 555.
[29] S. He, J. Luo, T.L. Liu, J. Mater, Inside Chem. 5 (2017) 12718.
[30] H. Nöth, R. Rurländer, P. Wolfgardt, Z. Naturforsch, B: Chem. Sci. 37 (1982) 29.
[31] A. Kitada, K. Nakamura, K. Fukami, K. Murase, Electrochim. Acta 211 (2016) 561.
[32] M.S. Sitze, E.R. Schreiter, E.V. Patterson, R.G. Freeman, Inorg. Chem. 40 (2001) 2298.
[33] Y.X. Fang, X.G. Jiang, X.G. Sun, S. Dai, Chem. Commun. 51 (2015) 13286.
[34] Y.X. Fang, K. Yoshii, X.G. Jiang, X.G. Sun, T. Tsuda, N. Mehio, S. Dai, Electrochim. Acta 160 (2015) 82.
[35] A. Kitada, K. Nakamura, K. Fukami, K. Murase, Electrochemistry 82 (2014) 946.
[36] A. Kitada, Y. Kato, K. Fukami, K. Murase, J. Surf, Finish. Soc. Jpn. 69 (2018) 310, https://doi.org/10.4139/sfj.69.310.
[37] Z.L. Zhang, A. Kitada, T.Y. Chen, K. Fukami, M. Shimizu, S. Arai, Z.J. Yao, K. Murase, J. Alloys Compd. 816 (2020).
[38] K. Murase, A. Ito, T. Ichii, H. Sugimura, D335, J. Electrochem. Soc. 158 (2011).
[39] P. Scherrer, Bestimmung der inneren Struktur und der Größe von Kolloidteilchen mittels Röntgenstrahlen, Kolloidchemie Ein Lehrbuch, Springer, 1912, p. 387.
[40] P. Lai, M. Skyllas-Kazacos, Electrochim. Acta 32 (1987) 1443.
[41] S. Wang, K.V. Kravchyk, F. Krumeich, M.V. Kovalenko, Acs Appl, Mater. Interfaces 9 (2017) 28478.
[42] A.P. Abbott, R.C. Harris, Y.T. Hsieh, K.S. Ryder, I.W. Sun, Phys. Chem. Chem. Phys. 16 (2014) 14675.
[43] N. Canever, N. Bertrand, T. Nann, Chem. Commun. 54 (2018) 11725.
[44] B. Scharifker, G. Hills, Electrochim. Acta 28 (1983) 879.
[45] T. Jiang, M.C. Brym, G. Dubé, A. Lasia, G. Brisard, Surf. Coating. Technol. 201 (2006) 10.
[46] P. Altimari, P.G. Schiavi, A. Rubino, F. Pagnanelli, J. Electroanal. Chem. 851 (2019) 113413.
[47] T. Zapryanova, A. Hrussanova, A. Milchev, J. Electroanal. Chem. 600 (2007) 311.
[48] O. Lebedeva, G. Jungurova, D. Kultin, L. Kustov, A. Zakharov, K. Kalmikov, E. Chernikova, V. Krasovskiy, Green Chem. 13 (2011) 1004.